RSC Advances

PAPER

View Article Online
View Journal | View Issue

Cite this: *RSC Adv.*, 2017, **7**, 52218

A novel strategy to promote photo-oxidative and reductive abilities *via* the construction of a bipolar Bi_2WO_6/N-$SrTiO_3$ material†

Huayu Gu,[a] Guanjie Xing,[b] Huimin Gu,[a] Zhanli Chai[a] and Xiaojing Wang *[a]

Focusing on holistically promoting both photo-oxidative and reductive abilities, we constructed a novel Bi_2WO_6/N-$SrTiO_3$ composite, which was expected to have excellent properties for the removal of complicated contaminants from solution environments under visible light irradiation. The prepared Bi_2WO_6/N-$SrTiO_3$ was assembled from massive N-$SrTiO_3$ nanoballs segmented *via* 2D interlaced nanosheets of Bi_2WO_6. N-$SrTiO_3$ on its own has good reductive ability and can easily reduce Cr(VI) ions, while Bi_2WO_6 has been demonstrated to have good oxidative ability to oxidize tetracycline under visible light irradiation. Importantly, mixed contaminants (TC and Cr^{6+} ions) could be completely removed under visible light by the assembled Bi_2WO_6/N-$SrTiO_3$ material. It is proposed that the holes lying at the valence band of N-$SrTiO_3$ are the main active species for the oxidation of tetracycline, while the electrons located at the conduction band of Bi_2WO_6 are mainly responsible for the reduction of Cr(VI) ions. The matched band structures of Bi_2WO_6 and N-$SrTiO_3$ were beneficial for inhibiting the recombination of electron–hole pairs and maintaining the redox capacity through a Z-type n–n heterojunction. Such a bipolar design of photo-oxidative and photo-reductive semiconductor nanomaterials is concluded to be highly effective in remediating complicated toxic residual constituents of both unfixed pharmaceuticals and heavy metals in aquatic environments.

Received 4th October 2017
Accepted 30th October 2017

DOI: 10.1039/c7ra10932f

rsc.li/rsc-advances

Introduction

Pollutants at low concentration but of high toxicity, such as antibiotic residues or heavy metal ions, have been increasingly found over recent years in aqueous environments and have been a subject of special concern.[1–3] They are potentially dangerous to ecosystems, and especially to human health, through drinking water and the food chain.[4,5] For example, many antibiotics can easily enter into the environment because of their poor absorption, low metabolism, abuse and overuse. The main issues lie in the large variety and quantities of both antibiotics and their intermediates present in the environment, which makes their remediation more difficult.[6,7] Aqueous heavy metal ions, being a common component of industrial waste with notoriously toxic, mutagenic and carcinogenic properties, could also lead to the deterioration of environmental quality and pose an acute threat to human health.[8–10] To summarize, the complexity of pollutants in water effluents means that it is imperative to develop an efficient technique that can simultaneously remove these residual antibiotics and heavy metals, rather than any single component.[11,12]

The semiconductor photocatalytic removal of toxic pollutants is considered to be the most promising strategy applicable, with the advantages of low cost, no secondary pollution, low energy consumption and environmental friendliness *via* the utilization of solar light.[13,14] Most of the photocatalytic systems only focus on a single function, either oxidative degradation or reductive elimination. However, in terms of practicality, the complexity of the pollutants that need to be removed inevitably leads to high requirements for photocatalysts with both outstanding oxidation and reduction properties. Therefore, there is an urgent need to find novel materials with excellent performance to completely eliminate mixed toxic residuals. Energetics dictates that for a semiconductor to be photochemically active, the oxidative potential of the photogenerated hole in the valence band must be sufficiently positive and the reductive potential of the conduction band electron must be sufficiently negative.[15] Although a single semiconductor with a big enough band gap may exhibit special redox abilities, the wide visible light response has inevitably to be sacrificed.[16,17] Another restriction in semiconductor photocatalysis is the relatively low value of the overall quantum efficiency, mainly due to the high recombination rate of photo-excited electron–hole pairs. To address these issues, the appropriate assembly of constituent semiconductors is believed to be one of the most

[a]*School of Chemistry and Chemical Engineering, Inner Mongolia University, Hohhot, Inner Mongolia, 010021, P. R. China. E-mail: wang_xiao_jing@hotmail.com*
[b]*School of Chemistry, Beijing Normal University, Beijing, 100875, P. R. China*

† Electronic supplementary information (ESI) available. See DOI: 10.1039/c7ra10932f

efficient strategies.[18,19] The electron–hole separation could be well enhanced by transferring electrons from a material with a high Fermi level to another material with a low Fermi level when they contact each other. Unfortunately, the oxidative potentials (and/or reductive potentials) are bound to increase (and/or decrease) to establish a thermodynamic equilibrium with the same Fermi level of the semiconductors at the interface.[20,21] Thereby, at present, uniting a broad spectrum of redox capabilities, visible light response, and recycling stability for composite fabrication is a still crucial challenge.

Strontium titanate (STO) has been used as one type of highly efficient photocatalyst, due to its outstanding optical and electrical performance, good conductivity and remarkable photochemical stability.[22] $SrTiO_3$ is a semiconductor with a wide band gap and its conductive band potential is about −0.4 eV, indicating its good reductive properties.[23,24] Through nitrogen doping (N-$SrTiO_3$), its disadvantage of a narrower adsorption region of the solar light spectrum was significantly improved.[25] It has been well proven that N-$SrTiO_3$ can efficiently reduce Cr(VI) ions under visible light. However, the recombination rate of the photoinduced electron–hole pairs in N-$SrTiO_3$ was faster than surface reductive reactions, leading to its deactivation after a few cycles. Moreover, the performance of N-$SrTiO_3$ for the oxidation of organic pollutants is still far from satisfactory. On the other hand, Bi-based semiconductor materials, such as Bi_2O_3, $Bi_4Ti_3O_{12}$, Bi_2WO_6, and Bi_2MoO_6, as novel kinds of photocatalysts have attracted much attention because of their layer structures and excellent catalytic properties. In particular, n-type semiconductor bismuth tungstate (Bi_2WO_6), with a valence band (VB) potential of 2.94 eV and a conduction band (CB) potential of 0.24 eV, is most interesting as a visible-light-responsive photocatalyst for the oxidative degradation of organic pollutants, owing to its excellent oxidation ability.[26–29] According to a recent report from Zhou *et al.*,[30] monolayer Bi_2WO_6 with a sandwich substructure serves as a layered heterojunction with holes generated on its active surface layer, leading to outstanding photocatalytic oxidative performance with good separation of electron–hole pairs. Huang *et al.*[31] also found that under visible light irradiation, Bi_2WO_6 could exhibit obvious photo-oxidative activity in pollutant degradation. A disadvantage of this nanomaterial is its poor reductive ability, due to the small negative potential of the conduction band.

In terms of their individual characteristics, the skilful incorporation of N-$SrTiO_3$ and Bi_2WO_6 may produce enhanced redox ability under visible light irradiation and efficiently accelerate electron–hole pair separation due to their matched band structure. In this work, a series of n–n heterojunctions of Bi_2WO_6/N-$SrTiO_3$ were successfully prepared through a two-step hydrothermal method. The removal rate of tetracycline, as a model sample for photocatalytic oxidation over the samples, was tested, while Cr(VI) ions were used as a model for the reductive ability. The redox abilities were further evaluated by simultaneous tetracycline oxidation and Cr(VI) ion reduction under visible light irradiation. Finally, a possible mechanism for the removal of mixed pollutants over Bi_2WO_6/N-$SrTiO_3$ was proposed.

Experimental

Material preparation and characterization

Preparation of N-$SrTiO_3$. The reagents were all analytical grade and used without further purification. N-$SrTiO_3$ powder was prepared using a hydrothermal method. The detailed procedure was provided in our previous work.[25]

Preparation of Bi_2WO_6/N-$SrTiO_3$. Bi_2WO_6/N-$SrTiO_3$ powder was prepared using a hydrothermal method. A certain amount of $Bi(NO_3)_3 \cdot 5H_2O$ was dissolved in 17 mL of deionized water, and $Na_2WO_4 \cdot 2H_2O$ was added to the above solution according to a molar ratio of 2 : 1. Then, 1 mL of HNO_3 (1 mol L^{-1}) was further added to the above mixture under magnetic stirring. Afterward, a certain amount of N-$SrTiO_3$ was added to the solution and stirring was continued for another 30 min. After that, the mixture was transferred into a Teflon-lined autoclave. The autoclave was sealed and maintained at 150 °C for 24 h. After cooling to room temperature in air naturally, the mixture was centrifuged and washed with distilled water and ethanol several times and then dried in air at 60 °C.[32] The mass ratio of Bi_2WO_6 to N-$SrTiO_3$ was set as 5, 8, 10, 15, and 20%, and the obtained samples were correspondingly labelled as Bi_2WO_6/NSTO5, Bi_2WO_6/NSTO8, Bi_2WO_6/NSTO10, Bi_2WO_6/NSTO15 and Bi_2WO_6/NSTO20, respectively.

Characterization. The phase structures and particle sizes of all of the as-prepared samples were characterized by X-ray power diffraction (XRD, PANalytical Empyream) with a copper gun. Samples morphologies were obtained using scanning electron microscopy (SEM), transmission electron microscopy (TEM) and high-resolution transmission electron microscopy (HRTEM) on a HITACHI S-4800 apparatus and a Tecnai G2F20S-TWIN apparatus with an acceleration voltage of 200 kV, respectively. A Perkin Elmer IR spectrometer was used to measure the frequencies of vibrations of surface groups of the as-prepared samples. The specific surface areas were determined from the nitrogen absorption data at liquid nitrogen temperature using the Barrett–Emmett–Teller (BET) technique on a Micromeritics ASAP 2000 Surface Area and Porosity Analyzer. Energy dispersive X-ray energy spectroscopy (EDS) was performed at an acceleration voltage of 20 kV on a HITACHI S-4800 apparatus. X-ray photoelectron spectroscopy (XPS) measurement was performed on a Thermo ESCALAB 250 with Al Kα (1486.6 eV) line at 150 W. To compensate for surface charge effects, the binding energies were calibrated using the C 1s peak at 284.60 eV as a reference. A diffusive reflectance UV-vis spectrophotometer (UVIKON XL/XS) was used to measure the diffuse reflectance spectra of the samples. $BaSO_4$ was taken as a reference, and the spectra were recorded in the range of 190–800 nm. The band gap of the samples was estimated from the onset of the absorption using the formula E_g (eV) = 1240/λ_g (nm). Electrochemical measurements were performed on a CHI 660D electrochemical workstation (Shanghai Chenhua, China) using a standard three-electrode cell with a working electrode, platinum wire as a counter electrode, and Ag/AgCl in saturated KCl as a reference electrode. Electrochemical impedance spectroscopy (EIS) was carried out at the open circuit potential. The

amplitude of the sinusoidal wave was 5 mV, and frequency range was from 100 kHz to 0.1 Hz. During all measurements, the electrolyte was 0.2 M Na_2SO_4. The charge transfer resistance of the materials was calculated by fitting the impedance data from the equivalent circuit using EIS.

Photocatalytic activity evaluation

The photocatalytic activities of the as-prepared samples were evaluated by tetracycline oxidation and Cr(VI) ion reduction. Tetracycline (TC) degradation was tested in a XPA-7 photochemical reactor containing 30 mg of catalyst sample and 100 mL of 20 mg L^{-1} tetracycline aqueous solution, which was adjusted to pH = 1. A 300 W Hg lamp with a UV-cutoff filter ($\lambda > 400$ nm) was placed inside the reactor. Water was circulated through the annulus to avoid heating during the reaction. The suspension was stirred continuously for 120 min in the dark to establish an equilibrium of tetracycline hydrochloride absorption/desorption on the samples before light irradiation. At certain time intervals, 4 mL of solution was centrifuged to investigate the changes in the absorption peak using a UVIKON XL/XS spectrometer and this was used to determine the concentration of TC. The photocatalytic degradation rate (D_r) was calculated using the following equation:

$$D_r = \frac{C_0 - C_t}{C_0} \times 100\% \quad (1)$$

where C_0 is the initial concentration of tetracycline solution and C_t is the concentration at irradiation time t.

Cr(VI) ion reduction was evaluated by analyzing the decreased concentration of Cr(VI) ions in the solution. 30 mg of catalyst sample was added into a $K_2Cr_2O_7$ aqueous solution (5 mg L^{-1}) together with the color-developing agent diphenylcarbazide (DPCI). The mixture solution was kept for 60 min in the dark, with constant stirring, to reach adsorption equilibrium. The reduction rate can be calculated according to the above eqn (1).

The synergic effect of removing both tetracycline and Cr(VI) ions was measured with similar photocatalytic activity experiments, by simultaneous degradation of a mixed solution containing tetracycline (20 mg L^{-1}) and Cr(VI) ions (5 mg L^{-1}) over 0.3 mg L^{-1} catalyst samples. The reactive active species were detected using trapping experiments. The process was similar to the above photodegradation experiments.

Results and discussion

Fig. 1 shows the XRD patterns of Bi_2WO_6/NSTO10 together with Bi_2WO_6 and N-$SrTiO_3$. The diffraction peaks of the Bi_2WO_6/NSTO10 composite were well matched to the standard values of the cubic phase of $SrTiO_3$ (ICOD no. 01-089-4934) and the tetragonal phase of Bi_2WO_6 (ICOD no. 01-079-2381). In addition, the characteristic peaks of Bi_2WO_6 were all weak in intensity in the as-prepared composites with different weight ratios of W : Ti = 5%, 8%, 10%, 15%, and 20%, respectively (Fig. S1†). This indicated the smaller amount of Bi_2WO_6 in the composites.[33] No other characteristic peaks were detected,

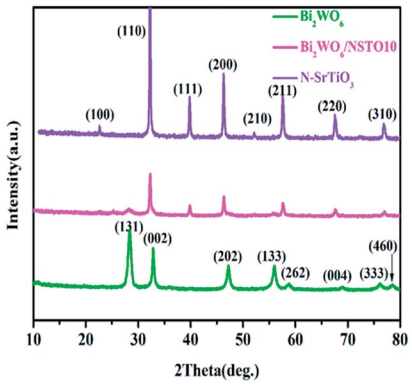

Fig. 1 XRD patterns of Bi_2WO_6/NSTO10, Bi_2WO_6, and N-$SrTiO_3$.

which demonstrated that Bi_2WO_6/N-$SrTiO_3$ composites were successfully fabricated without other impurities.

The morphologies of pure Bi_2WO_6, N-$SrTiO_3$ and Bi_2WO_6/NSTO10 were analyzed by scanning electron microscopy (SEM) and transmission electron microscopy (TEM). A good layer structure was observed visually for the prepared Bi_2WO_6, which was constructed from many 2D interlaced nanosheets (Fig. 2a). The N-$SrTiO_3$ particles exhibited a sphere-like shape with an average size of 30–50 nm, as shown in Fig. 2b. Fig. 2c intuitively indicated that nanosheets of Bi_2WO_6 were evenly inserted into the massive N-$SrTiO_3$ nanoballs. The HRTEM image of Bi_2WO_6/NSTO10 (Fig. 2d) clearly shows crystal lattice stripes with a spacing of 0.28 nm, corresponding to the (0 1 1) crystal plane of $SrTiO_3$ particles, while the lattice spacing of 0.31 nm was ascribed to the (1 3 1) crystal plane of Bi_2WO_6, in accordance with the XRD results. To further confirm the composition, the

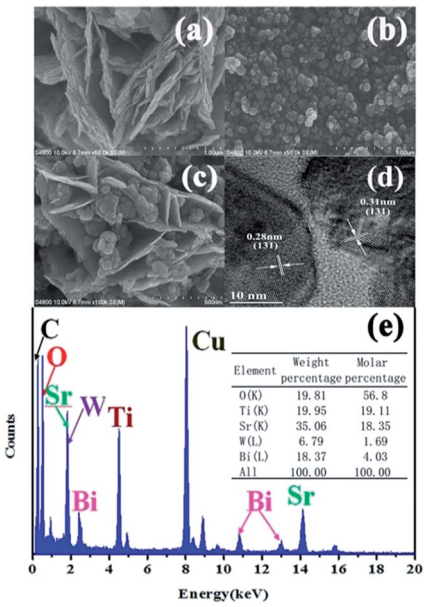

Fig. 2 SEM images of (a) Bi_2WO_6, (b) N-$SrTiO_3$, and (c) Bi_2WO_6/NSTO10, (d) HRTEM image of Bi_2WO_6/NSTO10, and (e) EDX spectrum of Bi_2WO_6/NSTO10, and EDS element content analysis of Bi_2WO_6/NSTO10 (inset).

element distribution of the as-prepared composite was analyzed by energy dispersive X-ray spectroscopy (EDS) (Fig. 2e). The existence of C, Cu, O, Sr, Ti, Bi, and W elements was observed in the EDS data, in which the C element was from the carbon film and Cu came from the copper wire mesh.[34] N was not detected, which was explained by the lower doping amount. From the inset of Fig. 2e, the atomic ratio of Sr/Ti is calculated to be approximately 1 : 1, very close to the theoretical value of $SrTiO_3$, while the atomic ratio of Bi/W is calculated to be approximately 2 : 1, corresponding to the theoretical value of Bi_2WO_6. Furthermore, the atomic ratio of W/Ti is close to 1 : 13, which is in agreement with the initial molar ratio of the composite. The growth process of Bi_2WO_6/N-$SrTiO_3$ could be approximately deduced and is schematically represented in Fig. S2.† The Bi_2WO_6 nanosheets were generated immediately when Bi^{3+} and WO_6^{6-} collided under hydrothermal reaction conditions. Then they were inserted into the massive as-prepared N-$SrTiO_3$ nanospheres to construct Bi_2WO_6/N-$SrTiO_3$, forming accumulated nano-balls segmented by nanosheets. This construction provided more active points for the adsorption of organic pollutants and separated redox active sites to completely remove the mixed pollutants through both oxidative degradation and reductive reaction.[35]

To investigate the light adsorption, UV-vis diffuse reflectance spectra of Bi_2WO_6, N-$SrTiO_3$, and Bi_2WO_6/N-$SrTiO_3$ composites with different W : Ti ratios were measured (Fig. 3a). Bi_2WO_6 exhibited light absorption from the UV to the visible light region, with an absorption edge at about 430 nm, which was assigned to the intrinsic band gap transition. N-$SrTiO_3$ showed a strong absorption in the range of 200–400 nm, as well as a stronger peak at around 420 nm. The optical absorption near the band edge follows the formula $(\alpha h\nu)^2 = A(h\nu - E_g)$, where α, h, ν, E_g, and A are the absorption coefficient, Planck's constant, the light frequency, the band gap, and a constant, respectively.[36] The band gap energy (E_g) is 2.83 eV for pure Bi_2WO_6 and 3.08 eV for N-$SrTiO_3$ as estimated by extrapolating the line (Fig. 3b), consistent with a previous study.[37,38] Apparently, compared with both pure Bi_2WO_6 and N-$SrTiO_3$, Bi_2WO_6/N-$SrTiO_3$ showed enhanced light absorption in the UV-vis region.

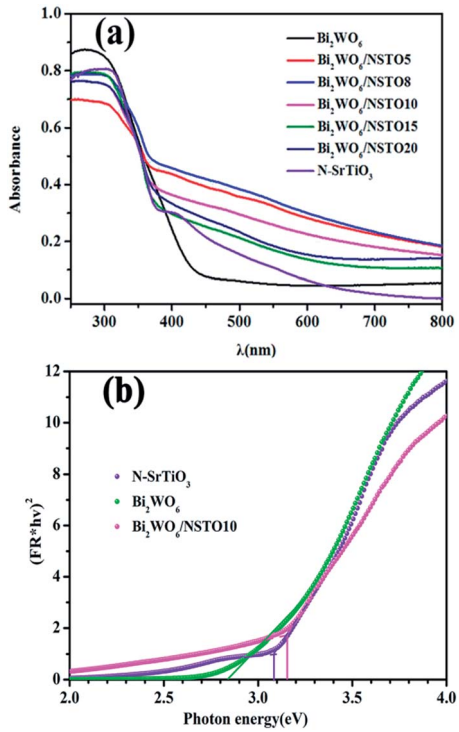

Fig. 3 (a) UV-visible diffuse reflectance spectra of the as-prepared samples, and (b) the optical bandgap of pristine Bi_2WO_6 and N-$SrTiO_3$.

The XPS results (Fig. 4) and FT-IR spectra (Fig. S3†) provided further insight into the chemical composition and groups of the as-prepared Bi_2WO_6 and Bi_2WO_6/NSTO10. The XPS survey spectra indicated the existence of Bi, O, W, Sr, Ti, and C elements in the surface of Bi_2WO_6/NSTO10 (Fig. 4a). The C 1s peak at a binding energy of about 284.9–285.9 eV is derived from the carbon tape used for fixing the sample and from atmospheric CO_2 adsorbed on the sample surface.[39] The high-resolution Bi 4f spectra of the Bi_2WO_6/NSTO10 and pure Bi_2WO_6 samples are shown in Fig. 4b. Two strong peaks located at 159.2 and 164.6 eV for both samples are attributed to Bi $4f_{7/2}$ and Bi $4f_{5/2}$ of Bi^{3+}, respectively. The peaks at binding energies of 35.4 and 37.5 eV are the signals of W $4f_{7/2}$ and $4f_{5/2}$ of W^{6+} in Bi_2WO_6 (Fig. 4c). In the same way, the binding energies of 132.6 and 134.4 eV with a doublet separation of 1.8 eV were assigned to $3d_{5/2}$ and $3d_{3/2}$ of Sr^{3+}, respectively (Fig. 4d).[40] The results indicate the consistent surface component of Bi^{3+} in the pure Bi_2WO_6 and Bi_2WO_6/NSTO10. The peaks in the FT-IR spectrum of Bi_2WO_6/NSTO10 were mainly matched with N-$SrTiO_3$ due to the enormous N-$SrTiO_3$ content in the composite (Fig. S4†). However, the peak at 1633 cm^{-1} was stronger in the composite than in the individual component, suggesting that the hydrophilic ability of the composite was enhanced.

TC was used as a model reagent to evaluate the oxidation ability of the as-prepared samples. Fig. 5a displays the UV

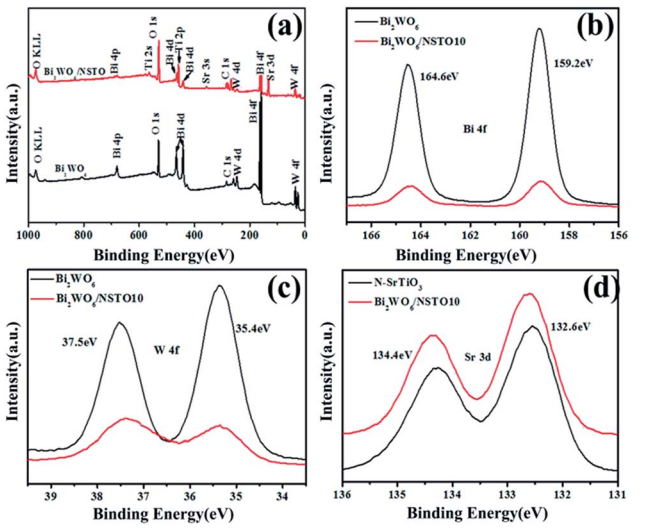

Fig. 4 The XPS spectra of Bi_2WO_6 and Bi_2WO_6/NSTO10: (a) survey, (b) Bi 4f orbitals, (c) W 4f orbitals, and (d) Sr 3d orbitals of N-$SrTiO_3$ and Bi_2WO_6/NSTO10.

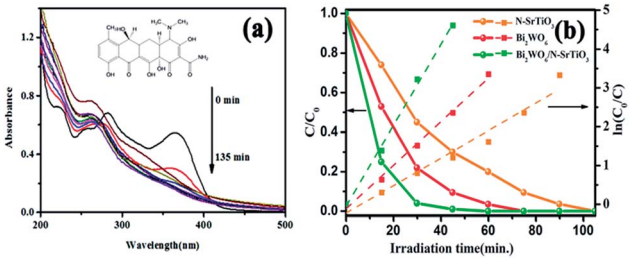

Fig. 5 (a) UV-vis absorption spectrum recorded during TC degradation over Bi_2WO_6/NSTO10 under visible light irradiation and structural formula of TC (inset). (b) Concentration of TC *versus* visible light irradiation time and the apparent reaction kinetic curve linear transformation.

spectra taken in the course of the photodegradation experiments of TC over Bi_2WO_6/NSTO10 under visible light illumination ($\lambda > 420$ nm). There is enough time in the dark for 2 h to ensure the establishment of an adsorption/desorption equilibrium of TC on the catalyst surface. A rapid decrease of TC at the wavelength of 360 nm was observed, accompanied by an absorption band shift to a shorter wavelength of 270 nm. The peaks at 270 nm and 360 nm corresponded to the E_2 and B bands of the benzene ring, respectively, indicating that the sample could degrade TC into small molecules.[41] In comparison with Bi_2WO_6 and N-$SrTiO_3$ in Fig. 5b, the conversion of TC was approximately 98% after 30 min of irradiation under visible light for Bi_2WO_6/N-$SrTiO_3$, higher than that of pure Bi_2WO_6 (79%) and N-$SrTiO_3$ (55%). According to the formula $\ln(C_0/C_t) = kt$, the lines were clearly well fitted with the pseudo-first-order kinetics model. The observed rate constant (k) for the degradation of TC is 5.76 h^{-1} for Bi_2WO_6/NSTO10, while that for N-$SrTiO_3$ is 2.91 h^{-1} and that for Bi_2WO_6 is 3.68 h^{-1}. It was proved that the oxidation of TC over Bi_2WO_6 surpassed that of N-$SrTiO_3$. More importantly, Bi_2WO_6/NSTO10 could gain an advantage over any sole component for the photocatalytic degradation of TC.

Cr(VI) ions were used as a model reagent to evaluate the reduction ability of the as-prepared samples. Fig. 6 shows the photo-reductive activities of Bi_2WO_6/N-$SrTiO_3$ composites together with pure Bi_2WO_6 and N-$SrTiO_3$. Opposite to TC oxidation, weak reduction (only 15%) was observed for Bi_2WO_6, whereas N-$SrTiO_3$ showed a higher photo-reductive efficiency (about 58% in 40 min) under visible light irradiation. Importantly, on assembling Bi_2WO_6 and N-$SrTiO_3$ (mass ratio from 5 to 10%), Bi_2WO_6/N-$SrTiO_3$ showed an obviously increased photo-reductive activity; 5 mg L^{-1} Cr(VI) ions were completely reduced in 90 min under visible light irradiation. However, it should be noted that when the mass ratio continues to increase (that is, the amount of Bi_2WO_6 becomes higher), there is a decrease in the photo-reductive activity. The kinetic rate constants under visible light were calculated (Fig. S4†). The photo-reduction of Cr(VI) ions can be fitted to a pseudo-first-order reaction and the rate constant (k_{ap}) is 2.33 h^{-1} for Bi_2WO_6/NSTO10, obviously higher than that of N-$SrTiO_3$ (0.908 h^{-1}) and Bi_2WO_6 (0.155 h^{-1}). As a result, the constructed heterojunction of Bi_2WO_6/NSTO10 presented the highest photo-reductive activity compared with either component.

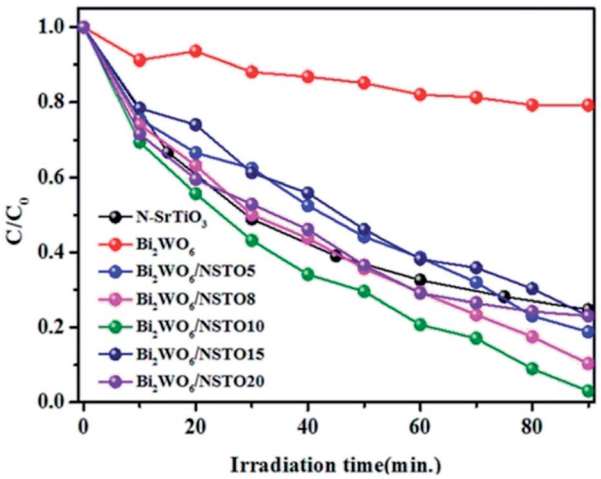

Fig. 6 Concentration of Cr(VI) *versus* visible light irradiation time in the presence of Bi_2WO_6, N-$SrTiO_3$ and Bi_2WO_6/N-$SrTiO_3$ with various ratios of W : Ti = 5%, 8%, 10%, 15%, and 20%, respectively.

Finally, the feasibility of simultaneous tetracycline oxidation and Cr(VI) ion reduction over Bi_2WO_6/N-$SrTiO_3$ was tested in a simulated complicated solution that contained tetracycline and Cr(VI) ions. Firstly, the reduction rate of Cr(VI) ions in the mixed solution is shown in Fig. 7a. The Cr(VI) ions (5 mg L^{-1}) were completely reduced in 20 min under visible light for the Bi_2WO_6/NSTO10 composite, which is about 2 and 10 times faster than the reaction with pure N-$SrTiO_3$ and Bi_2WO_6, respectively. Secondly, the oxidation of TC in the mixed solution is shown in Fig. 7b. For Bi_2WO_6/NSTO10, the oxidation of TC was accelerated in the mixture of Cr(VI) and TC under visible light, and up to 100% of the TC was oxidized within 20 min, indicating about 1.45 and 2.5 times better activity than the sole

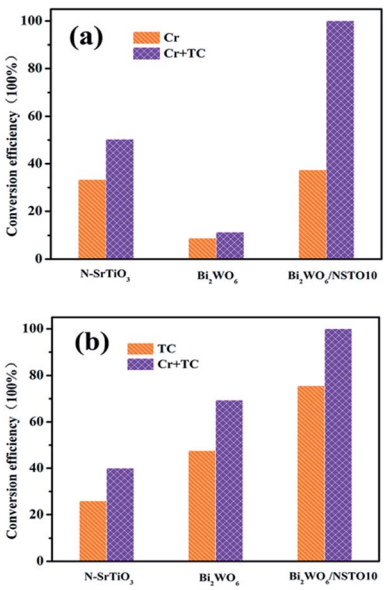

Fig. 7 (a) Cr(VI) and (b) TC conversion efficiencies in the first 20 minutes over the as-prepared photocatalysts in a single solution (TC or Cr(VI)) and mixed solution (TC and Cr(VI)).

components Bi_2WO_6 (69%) and N-$SrTiO_3$ (40%). Thirdly, all samples, Bi_2WO_6/NSTO10, Bi_2WO_6, and N-$SrTiO_3$, showed better activity for TC oxidation (or Cr^{6+} ion reduction) in the mixed pollutant environment than in the single pollutant solution. Thus, two conclusions were derived from the above results. (1) The integrated Bi_2WO_6/N-$SrTiO_3$ composite was obviously more efficient for both TC oxidation and Cr(VI) ion reduction than any sole component, indicating that both the oxidative and reductive performance were substantially improved through coupling design. (2) The coexistence of tetracycline and Cr(VI) ions was conducive to the removal of either constituent contaminant, confirming that the designed Bi_2WO_6/N-$SrTiO_3$ was absolutely superior for the removal of mixed contaminants. Besides, compared with other references regarding the photocatalytic reduction of Cr(VI) ions[42–45] and the degradation of TC,[46–48] the removal efficiency of the present work showed outstanding advantages (Tables S1 and S2†).

To assess the stability of the as-prepared composite, the photocurrent under 300 W xenon lamp irradiation was recorded and shown in Fig. 8a. Among all the samples, N-$SrTiO_3$ presented the highest photocurrent density, implying higher light harvesting. However, the photocurrent response was continuously decreased during several on–off cycles. Combining Bi_2WO_6 and N-$SrTiO_3$ into a composite, the photo-responsive phenomenon of Bi_2WO_6/NSTO10 was entirely reversible upon each light irradiation, exhibiting more excellent stability. We also conducted recycling experiments for the mixed contaminants over Bi_2WO_6/NSTO10 under visible light irradiation and the results are illustrated in Fig. 8b. No noticeable activity change is observed during four successive cycles, suggesting that the Bi_2WO_6/NSTO10 composite is recyclable with good stability during the photocatalytic remediation of complicated toxic residuals.

As is well known, the specific surface area and porosity are important factors to enhance catalytic performance. The isotherm curves of Bi_2WO_6, N-$SrTiO_3$, and Bi_2WO_6/NSTO10 were characterized as type III with an H_3 hysteresis loop according to Brunauer–Deming–Deming–Teller (BDDT) classification,[49] as shown in Fig. 9. The BET surface area of the Bi_2WO_6/NSTO10 nanocrystals is about 31.0 $cm^3\ g^{-1}$, slightly larger than the value of 27.7 $cm^3\ g^{-1}$ for N-$SrTiO_3$, whereas it is obviously smaller than that of Bi_2WO_6 (inset of Fig. 9). Combined with the photocatalytic results (Fig. 8), it was deduced that the change in electron structure played a significant role in enhancing the photocatalytic performance, instead of the high BET surface area in the as-prepared composite.

Radical-trapping experiments were performed to determine the active species in TC degradation by using different scavengers, including benzoquinone (BQ, superoxide anion O^{2-} radical scavenger), *tert*-butanol (TBA, $^{\bullet}OH$ radical scavenger), silver nitrate ($AgNO_3$, electron scavenger) and ammonium oxalate (AO, hole scavenger).[50] As shown in Fig. 10, TC photodegradation was greatly restrained in the presence of AO, compared with the reaction without radical scavengers. Furthermore, the degradation of TC was slightly decreased when TBA was added into the reaction system. These results revealed that h^+ plays a more significant role, while $^{\bullet}OH$ gives a secondary contribution in TC degradation under visible light irradiation, confirming that an oxidative reaction of TC occurred for Bi_2WO_6/NSTO10 in aqueous solution.

EIS is an efficient electrochemical method to explain the electron-transfer efficiency at electrodes.[51] N-$SrTiO_3$ showed the biggest diameter, implying that it has poor electrical conductivity (Fig. 11a). In comparison, Bi_2WO_6/NSTO10 exhibited the smallest diameter, indicating a faster charge transfer shift through the composite electrode interface. This suggested a significant promotion of the photo-response ability due to the effective restraint of photo-generated charge recombination. The charge transfer resistance of the materials was obtained

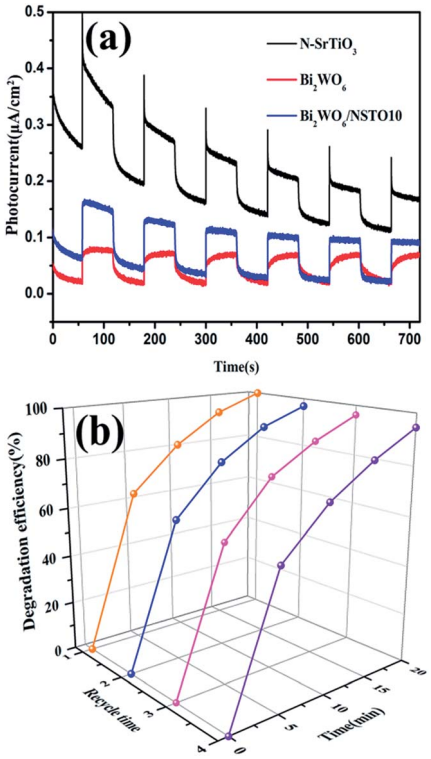

Fig. 8 (a) Photocurrent responses of N-$SrTiO_3$, Bi_2WO_6 and Bi_2WO_6/NSTO10 electrodes. (b) Cycling degradation of TC in a mixed solution (TC and Cr(VI)) using Bi_2WO_6/NSTO10.

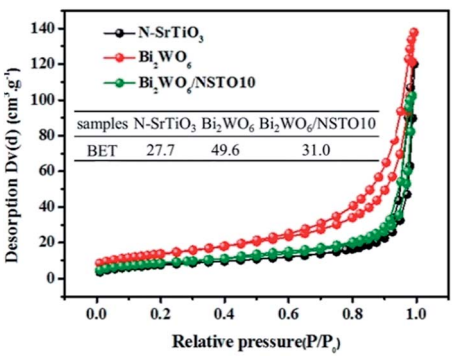

Fig. 9 Nitrogen adsorption/desorption isotherms and BET of the as-prepared samples (inset).

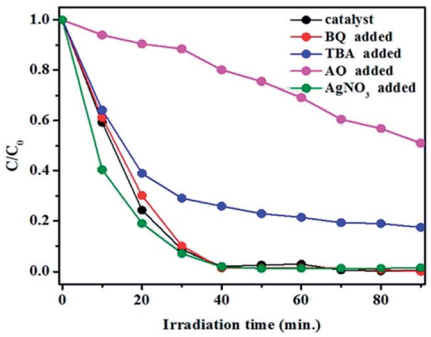

Fig. 10 Effects of different scavengers on TC degradation in the presence of Bi_2WO_6/NSTO10 under visible light irradiation.

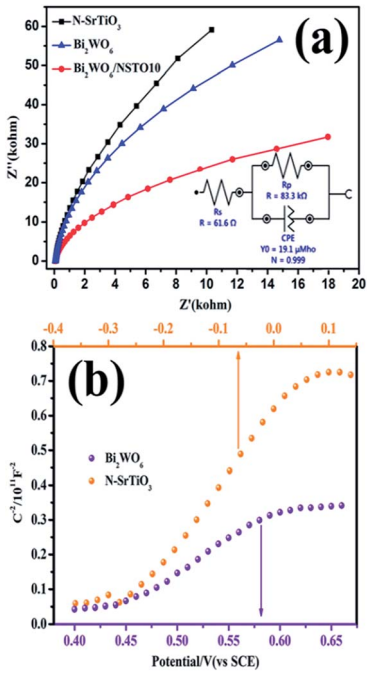

Fig. 11 (a) Electrochemical impedance spectroscopy (EIS) plots, and (b) Mott–Schottky (MS) plots of the Bi_2WO_6 and N-$SrTiO_3$ film electrodes.

from the equivalent circuit by fitting the impedance data using EIS. The fitted impedance value of Bi_2WO_6/NSTO10 (83.3 kΩ) is smaller than that of Bi_2WO_6 (136 kΩ) or N-$SrTiO_3$ (184 kΩ) alone, attributed to the accelerated formation of charge-transfer states and depletion layers within the nanocomposites through the internal electrostatic field in the heterojunction. The reduced resistance of Bi_2WO_6/N-$SrTiO_3$ suggested an increased transmission rate of photogenerated charge carriers. Fig. 11b shows the electrochemical Mott–Schottky plot of Bi_2WO_6 and N-$SrTiO_3$ films on a platinum electrode substrate. The positive slopes revealed a typical n-type characteristic for both Bi_2WO_6 and N-$SrTiO_3$. Thus, a Z-type n–n heterojunction is constructed by assembling N-$SrTiO_3$ and Bi_2WO_6, in which the conduction band potential is −0.28 eV for N-$SrTiO_3$ and 0.43 eV of Bi_2WO_6, respectively, in terms of the equivalence of the Fermi level and conduction band potential in an n-type semiconductor. According to the band gaps of N-$SrTiO_3$ (3.08 eV) and Bi_2WO_6 (2.83 eV), their valence band (E_{VB}) positions are estimated to be 2.80 and 3.26 eV, respectively. Based on the above experiment, the probable mechanism for the photocatalytic removal of the mixed tetracycline and Cr(VI) ions over Bi_2WO_6/N-$SrTiO_3$ under visible light irradiation is described in Fig. 12. (1) Under visible light illumination, electrons (e^-) are excited into the CB and holes located at the valence band of N-$SrTiO_3$. The same occurs for Bi_2WO_6. (2) The conduction band potentials of Bi_2WO_6 and N-$SrTiO_3$ are higher compared with the reductive potential of $Cr_2O_7^{2-}/Cr^{3+}$ (1.27 eV *versus* NHE), and thus they both exhibit reducing capacity for Cr(VI) to Cr(III) ions, which was demonstrated in the Cr(VI) reduction experiment. However, N-$SrTiO_3$ exhibited excellent reducing ability due to its high conduction band level, whereas the reducing activity of Bi_2WO_6 was poor due to its slightly lower conduction band compared to N-$SrTiO_3$ (Fig. 7). (3) On the other hand, the valence band potentials of N-$SrTiO_3$ and Bi_2WO_6 are all lower than the oxidation potential of TC (−3.28 eV), as shown in Fig. S5.† As a result, the holes in the valence band of N-$SrTiO_3$ and Bi_2WO_6 could degrade TC directly. However, the valence band potential of Bi_2WO_6 is much lower than the redox potential of $^{\cdot}OH/H_2O$ (2.73 eV *versus* NHE), indicating that its holes could transform H_2O into $^{\cdot}OH$ and then oxidize TC. This was confirmed by the radical-trapping experimental results. At the same time, N-$SrTiO_3$ exhibits poor performance for the oxidation of TC due to its not very low valence band energy. (4) If we combine the two separate components, band bending was not obvious, due to the close Fermi energy level in the present n–n junction. The conduction band (CB) of Bi_2WO_6 was slightly shifted upwards. In this case, the redox abilities of each component were not changed very much, unlike in p–n type junctions.[20,21] As a result, while maintaining the greater transition tendency of the charges between Bi_2WO_6 and N-$SrTiO_3$, the reductive ability of N-$SrTiO_3$ did not obviously decrease. The same case is observed for the oxidative performance of Bi_2WO_6.[52] Therefore, the photogenerated charge carriers are effectively separated by the heterojunction between Bi_2WO_6 and N-$SrTiO_3$, and the photocatalytic activity is also significantly improved.

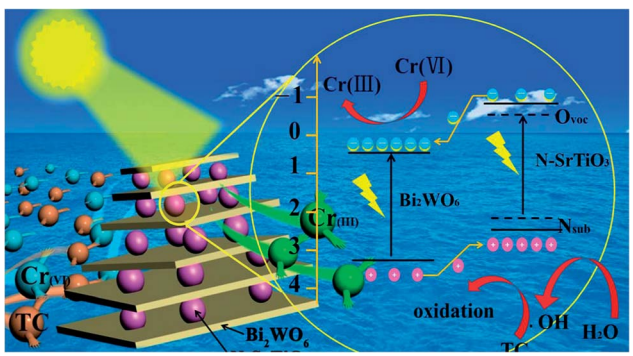

Fig. 12 Possible mechanism for Cr(VI) photoreduction and tetracycline oxidation over the Bi_2WO_6/NSTO10 photocatalytic system under visible light irradiation.

Conclusions

In summary, we have successfully fabricated a series of n–n Bi_2WO_6/N-$SrTiO_3$ heterojunctions with different mass ratios of W to Ti using a hydrothermal method. The as-prepared samples were composed of massive N-$SrTiO_3$ nanoballs with a diameter of about 10–20 nm, segmented by a small amount of 2D interlaced Bi_2WO_6 nanosheets. As established in the UV-vis experiment, the capacity to absorb visible light was significantly improved in the composite. Moreover, this Bi_2WO_6/N-$SrTiO_3$ composite showed obviously superior visible light photocatalytic efficiency and stability for the simultaneous removal of tetracycline and Cr(VI) compared with the individual Bi_2WO_6 or N-$SrTiO_3$, confirming that the high reductive and oxidative ability could be holistically improved through coupling design. This is particularly useful for the remediation of mixed contaminants in complicated aquatic environments. The results of free radical trapping experiments revealed that photo-excited h^+ and e^- were responsible for the oxidation of TC and reduction of Cr(VI) ions, respectively. The Z type n–n heterojunction of Bi_2WO_6/N-$SrTiO_3$ exhibited an excellent bipolar photo-oxidative and photo-reductive ability, while retaining a good visible light response, and simultaneously promoted the separation of the photogenerated electron–hole pairs. The present work could offer a new strategy to develop more efficient binary catalysts for practical application in the elimination of pharmaceutical and heavy metal pollutants in aquatic environments.

Conflicts of interest

There are no conflicts to declare.

Acknowledgements

This work was financially supported by the National Natural Science Foundation of China (Grants 21567017 and 21777078), the open project of the state key laboratory of inorganic synthesis and preparative chemistry of Jilin University (2016-10), and the Project of Research and Development of the Applied Technology for Inner Mongolia 2017.

References

1 R. Hirsch, T. Ternes, K. Haberer and K. Kratz, *Sci. Total Environ.*, 1999, **225**(1–2), 109–118.
2 B. Li and T. Zhang, *Water Res.*, 2013, **47**, 2970–2982.
3 A. Sarmah, M. Meyer and A. Boxall, *Chemosphere*, 2006, **65**(5), 725–759.
4 J. Bound and N. Voulvoulis, *Chemosphere*, 2004, **56**(11), 1143–1155.
5 T. Wang, W. Liu, L. Xiong, N. Xu and J. Ni, *Chem. Eng. J.*, 2013, **215–216**, 366–374.
6 X. Yu, Z. Lu, D. Wu, P. Yu, M. He, T. Chen, W. Shi, P. Huo, Y. Yan and Y. Feng, *React. Kinet., Mech. Catal.*, 2014, **111**, 347–360.
7 L. Minh, N. Khan, J. Drewes and R. Stuetz, *Water Res.*, 2010, **44**, 4295–4323.
8 T. Aarthi and G. Madras, *Catal. Commun.*, 2008, **9**(5), 630–634.
9 D. Kolpin, E. Furlong, M. Meyer, E. Thurman, S. Zaugg, L. Barber and H. Buxton, *Environ. Sci. Technol.*, 2002, **36**, 1202–1211.
10 Q. Yuan, L. Chen, M. Xiong, J. He, S. Luo, C. Au and S. Yin, *Chem. Eng. J.*, 2014, **255**, 394–402.
11 F. Lian, Z. Song, Z. Liu, L. Zhu and B. Xing, *Environ. Sci. Pollut. Res.*, 2013, **178**, 264–270.
12 Z. Zhang, H. Liu, L. Wu, H. Lan and J. Qu, *Chemosphere*, 2015, **138**, 625–632.
13 T. Yan, J. Tian, W. Guan, Z. Qiao, W. Li, J. You and B. Huang, *Appl. Catal., B*, 2017, **202**, 84–94.
14 P. Huo, M. Zhou, Y. Tang, X. Liu, C. Ma, L. Yu and Y. Yan, *J. Alloys Compd.*, 2016, **670**, 198–209.
15 D. Ma, J. Wu, M. Gao, Y. Xin, T. Ma and Y. Sun, *Chem. Eng. J.*, 2016, **290**, 136–146.
16 X. Liu, Q. Lu and J. Liu, *J. Alloys Compd.*, 2016, **662**, 598–606.
17 P. Ju, Y. Wang, Y. Sun and D. Zhang, *Dalton Trans.*, 2016, **45**, 4588–4602.
18 Y. Xiang, P. Ju, Y. Wang, Y. Sun, D. Zhang and J. Yu, *Chem. Eng. J.*, 2016, **288**, 264–275.
19 X. Wang, S. Li, Y. Ma, H. Yu and J. Yu, *J. Phys. Chem. C*, 2011, **115**(30), 14648–14655.
20 Y. Zhang, Y. Yu, X. Wang, G. Tong, L. Mi, Z. Zhu, X. Geng and Y. Jiang, *J. Mater. Chem. C*, 2017, **5**, 140–148.
21 N. Zhang, Y. Zhang, X. Pan, M. Yang and Y. Xu, *J. Phys. Chem. C*, 2012, **116**, 18023–18031.
22 K. Yu, C. Zhang, Y. Chang, Y. Feng, Z. Yang, T. Yang, L. Lou and S. Liu, *Appl. Catal., B*, 2017, **200**, 514–520.
23 C. Zhang, K. Yu, Y. Feng, Y. Chang, T. Yang, Y. Xuan, D. Lei, L. Lou and S. Liu, *Appl. Catal., B*, 2017, **210**, 77–87.
24 W. Dong, X. Li, J. Yu, W. Guo, B. Li, L. Tan, C. Li, J. Shi and G. Wang, *Mater. Lett.*, 2012, **67**, 131–134.
25 G. Xing, L. Zhao, T. Sun, Y. Su and X. Wang, *SpringerPlus*, 2016, **5**, 1132.
26 W. Chen, T. Liu, T. Huang, X. Liu, J. Zhu, G. Duan and X. Yang, *Appl. Surf. Sci.*, 2015, **355**, 379–387.
27 J. Zhu, S. Liu, Q. Yang, P. Xu, J. Ge and X. Guo, *Colloids Surf., A*, 2016, **489**, 275–281.
28 M. Li, L. Zhang, X. Fan, Y. Zhou, M. Wu and J. Shi, *J. Mater. Chem. A*, 2015, **3**(9), 5189–5196.
29 D. Yue, D. Chen, Z. Wang, H. Ding, R. Zong and Y. Zhu, *Phys. Chem. Chem. Phys.*, 2014, **16**, 26314.
30 Y. Zhou, Y. Zhang, M. Lin, J. Long, Z. Zhang, H. Lin, J. Wu and X. Wang, *Nat. Commun.*, 2015, **6**, 8340.
31 Y. Huang, S. Kang, Y. Yang, H. Qin, Z. Ni, S. Yang and X. Li, *Appl. Catal., B*, 2016, **196**, 89–99.
32 J. Xu, Y. Wei, Y. Huang, J. Wang, X. Zheng, Z. Sun, L. Fan and J. Wu, *Ceram. Int.*, 2014, **40**, 10583–10591.
33 L. Chen, D. Jiang, T. He, Z. Wu and M. Chen, *CrystEngComm*, 2013, **15**(37), 7556–7563.
34 M. Sun, D. Li, W. Zhang, Z. Chen, H. Huang, W. Li, Y. He and X. Fu, *J. Phys. Chem. C*, 2009, **113**, 14916–14921.

35 L. Qu, J. Lang, S. Wang, Z. Chai, Y. Su and X. Wang, *Appl. Surf. Sci.*, 2016, **388**, 412–419.
36 L. Ye, X. Jin, C. Liu, C. Ding, H. Xie, K. Chu and P. Wong, *Appl. Catal., B*, 2016, **187**, 281–290.
37 S. Kumar, S. Tonda, A. Baruah, B. Kumar and V. Shanker, *Dalton Trans.*, 2014, **43**, 16105–16114.
38 J. Li, H. Hao and Z. Zhu, *Mater. Lett.*, 2016, **168**, 180–183.
39 H. Li, Q. Deng, J. Liu, W. Hou, N. Du, R. Zhang and X. Tao, *Catal. Sci. Technol.*, 2014, **4**, 1028–1037.
40 L. Zhang, W. Tian, Y. Chen, J. Chen, H. Teng, J. Zhou, J. Shi and Y. Sun, *RSC Adv.*, 2016, **6**, 83471.
41 M. Liu, G. Lv, L. Mei, X. Wang, X. Xing and L. Liao, *Adv. Mater. Sci. Eng.*, 2014, **2014**, 409086.
42 H. Xu, W. Zhang, M. Ding and X. Gao, *Mater. Des.*, 2017, **114**, 129–138.
43 L. Liu, C. Luo, J. Xiong, Z. Yang, Y. Zhang, Y. Cai and H. Gu, *J. Alloys Compd.*, 2017, **690**, 771–776.
44 J. Qu, D. Chen, N. Li, Q. Xu, H. Li, J. He and J. Lu, *Appl. Catal., B*, 2017, **207**, 404–411.
45 M. Naimi-Joubani, M. Shirzad-Siboni, J. K. Yang, M. Gholami and M. Farzadkia, *J. Chem. Eng.*, 2015, **22**, 317–323.
46 M. Cao, P. Wang, Y. Ao, W. Chao, J. Hou and Q. Jin, *J. Colloid Interface Sci.*, 2016, **467**, 129–139.
47 P. Huo, Z. Ye, H. Wang, Q. Guan and Y. Yan, *J. Alloys Compd.*, 2017, **696**, 701–710.
48 Z. Ye, J. Li, M. Zhou, H. Wang, Y. Ma, P. Huo, L. Yu and Y. Yan, *Chem. Eng. J.*, 2016, **304**, 917–933.
49 Y. Su, L. Hou, C. Du, L. Peng, K. Guan and X. Wang, *RSC Adv.*, 2012, **2**, 6266.
50 B. Luo, D. Xu, D. Li, G. Wu, M. Wu, W. Shi and M. Chen, *ACS Appl. Mater. Interfaces*, 2015, **7**, 17061–17069.
51 S. Zhang, J. Li, M. Zeng, G. Zhao, J. Xu, W. Hu and X. Wang, *ACS Appl. Mater. Interfaces*, 2013, **5**, 12735–12743.
52 J. Lee, Y. Kim, J. Kim, S. Kim, D. Min and D. Jang, *Appl. Catal., B*, 2017, **205**, 433–442.